J Mater Sci (2026) 61:6754–6767

Computation & theory

Comprehensive analysis of structural, mechanical, electronic, optical, and thermodynamic properties of an alternative semiconductor: Ti_2MnCoS_2 double half Heusler

Meryem Yurt[1,2], Evren Görkem Özdemir[1,*], Wisam A. A. Ahmed[1,2], and H. A. Rahnamaye Aliabad[3]

[1] *Department of Physics, Faculty of Science, Gazi University, Teknikokullar, 06560 Ankara, Türkiye*
[2] *Department of Physics, Graduate School of Natural and Applied Sciences, Gazi University, Teknikokullar, 06560 Ankara, Türkiye*
[3] *Department of Physics, Hakim Sabzevari University, Sabzevar, Iran*

Received: 5 January 2026
Accepted: 20 January 2026
Published online: 3 February 2026

© The Author(s), 2026

ABSTRACT

The comprehensive investments of Ti_2MnCoS_2 Double Half Heusler (DHH) alloy were studied using first-principles calculations. The electronic properties indicate that the Ti_2MnCoS_2 DHH alloy exhibits semiconductor behavior. The equilibrium lattice parameters are a = b = 5.48 Å and c = 10.96 Å. The band gap values at these parameters are 0.840 eV and 1.007 eV for the GGA and GGA + mBJ approximations, respectively. The bulk modulus values were obtained as 173.4365 GPa, 165.655 GPa, and 169.752 GPa in structural, elastic, and thermodynamic calculations, respectively. These similarities demonstrate the consistency of the calculations for Ti_2MnCoS_2 semiconductor DHH alloy. The alloy is mechanically stable and ductile with a Poisson's ratio of 0.281. The optical properties reveal that the material exhibits not only its electronic properties but also interesting characteristics under light, particularly in the visible light region. Thermodynamic calculations confirmed its structural stability under varying pressure and temperature. Elastic calculations determined the Debye temperature to be 543.076 K. Thermodynamic data also showed a value of 582.57 K at 0 GPa and 0 K. The Gibbs energy curve indicates that the Ti_2MnCoS_2 semiconductor DHH alloy maintains structural stability across different external conditions.

Handling Editor: Kevin Jones.

Address correspondence to E-mail: evrengorkemozdemir@gazi.edu.tr

https://doi.org/10.1007/s10853-026-12291-0

Introduction

Heusler compounds, discovered by Heusler in 1903 and named after him [1, 2], have become one of the frequently used groups in materials technology due to their consistency and ease of calculation in both experimental and theoretical calculations [3–8]. Heusler compounds can be classified into three categories: full-Heusler (X_2YZ) [9–12], half-Heusler (XYZ) [13–16], and quaternary Heusler (XX^1YZ) [17–20]. Here, X, X^1, and Y are transition metals, and Z is a III-VI A group element. Heusler compounds are one of the frequently used material groups, especially in spintronics applications, because these materials exhibit high spin polarization around the Fermi energy levels. Spintronics is a branch of science that includes devices based on the spin orientations of nanoscale materials. Heusler compounds have become an interesting material in spintronics applications since the NiMnSb Heusler compound was obtained by de Groot [21] as a half-metallic material with 100% spin polarization.

Double half-Heusler (DHH) alloys have also gained a place among spintronic and semiconductor technologies in recent years due to the properties they have demonstrated. Their structural formula is $X_2X^1YZ_2$ [22, 23]. In 2022, Ding et al. [24] conducted research on the $Mn_2FeCoSi_2$ DHH alloy. The molecular structure of the $Mn_2FeCoSi_2$ DHH alloy was produced in the I-42d symmetry group. The equilibrium point lattice parameters a = b = 5.36 Å and c = 10.72 Å were obtained. This alloy exhibits metallic character in spin-up states and semiconducting character with a band gap of 0.54 eV in spin-down states, thereby qualifying it as a true half-metallic alloy. The total magnetic moment was calculated to be 3.00 μ_B. This integer magnetic moment value is an expected result for true half-metallic materials. In 2021, Uğur et al. [25] investigated the structural and electronic properties of $Ti_2FeNiSb_2$ and Ti_2Ni_2InSb DHH alloys. The alloys were synthesized in the I-42d symmetry group. $Ti_2FeNiSb_2$ and Ti_2Ni_2InSb DHH alloys have typical semiconducting properties. The band gap values are 0.63 eV and 0.42 eV, respectively. $Ti_2FeNiSb_2$ and Ti_2Ni_2InSb tetragonal DHH alloys met the elastic stability conditions and were obtained as ductile semiconductor materials. In addition, Hasan et al. investigated the changes in the thermoelectric properties of the $Ti_2FeNiSb_2$ DHH alloy by atomic doping [26]. In this study, Co and Bi atoms were added to Fe and Sb atoms at 0.025, 0.050, 0.075, and 0.10%. At these ratios, the $Ti_2Fe_{0.9}Co_{0.1}NiSb_2$ alloy achieved a 0.69 zT value, significantly higher than that of pure $Ti_2FeNiSb_2$. The properties of Cr-based Cr_2FeCoZ_2 (Z = As, Ge, S, P) DHH alloys were investigated by Zhao et al. [27]. These alloys were synthesized by placing the coordinates of Cr, Fe, Co, and Z atoms at space number 122 as 0.75, 0.75, 0.625/0, 0, 0.5/0, 0, 0/0.25, 0.75, 0.625, respectively. The materials are ferrimagnetic due to the antiparallel magnetic orientations of Cr, Fe, and Co atoms. According to their electronic properties, the alloys exhibit half-metallic behavior. The largest band gap at the equilibrium lattice point is found in the $Cr_2FeCoAs_2$ alloy, with a value of 1.181 eV. When the Cr_2FeCoZ_2/GaAs/Cr_2FeCoZ_2 states are used as left and right electrodes, the transport capacities of the magnetic tunnel junctions (MTJs) obtained when the magnetic arrays are antiparallel are significantly reduced. It was also observed that the transport of electrons in spin-up states is increased dramatically when the magnetic arrays are arranged parallel to the right and left electrodes. The MTJ structure obtained with the $Cr_2FeCoAs_2$/GaAs/$Cr_2FeCoAs_2$ DHH alloy has the highest tunneling magnetoresistance.

As can be seen from the examples provided, DHH alloys are a group of materials that have gained a significant place in a wide range of fields, both experimentally and theoretically. Consistent theoretical calculations of DHH alloys and their demonstrated properties make them remarkable materials. Our primary motivation for this study was to conduct a comprehensive investigation of the Ti_2MnCoS_2 DHH alloy, whose properties were thoroughly examined, along with the stability of its electronic and structural properties, as supported by mechanical calculations, and its semiconductor nature, which could shed light on various areas of the literature.

Calculation method

First-principles studies of the Ti_2MnCoS_2 semiconductor DHH alloy were completed using the Wien2k program, developed by Blaha et al., which performs calculations within the DFT framework [28, 29]. The space number 122 and the I-42d symmetry group were selected for the alloy. The atomic positions for Ti, Mn, Co, and S were determined as 0.75/0.75/0.625, 0/0/0.50, 0/0/0, and 0.25/0.75/0.625, respectively. The lattice parameters were selected as a = b and c = 2a, creating the molecular structure shown in

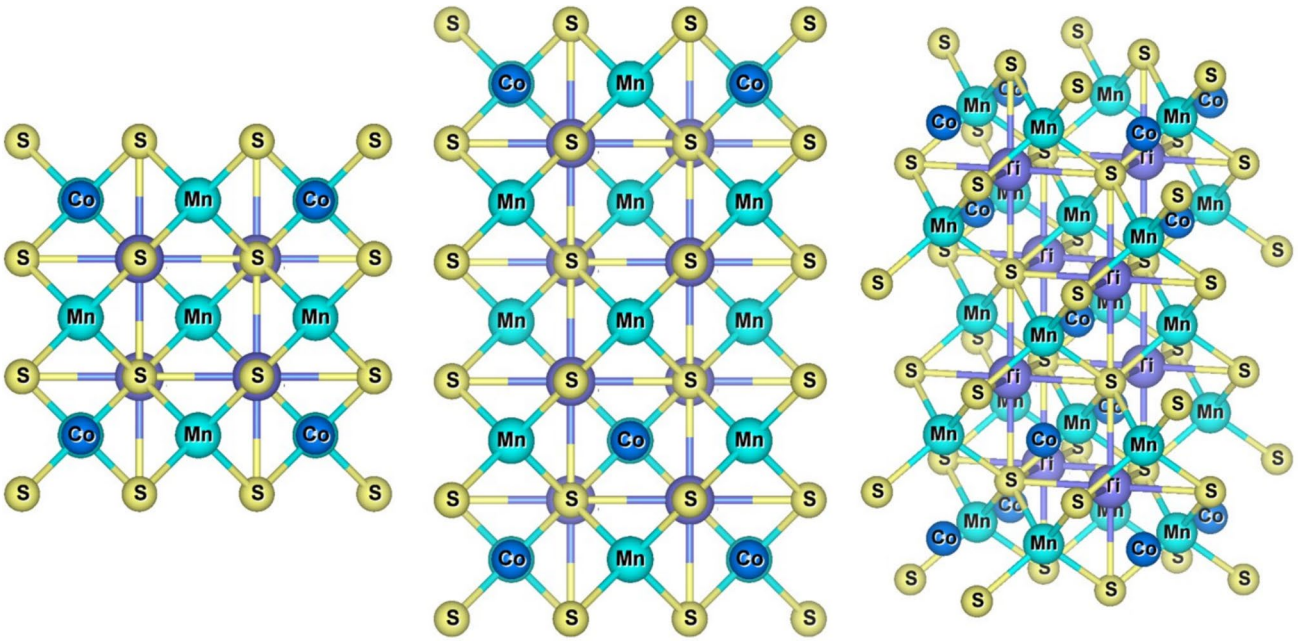

Figure 1 The molecular structure of the Ti_2MnCoS_2 double half-Heusler was created by VESTA [30].

Fig. 1. All properties of the Ti_2MnCoS_2 double half-Heusler alloy were calculated based on the created structure in Fig. 1. Ground-state calculations were performed here using the GGA + PBE approximation [31]. To determine the convergence properties, 12 × 12x12 k-points were determined for the system, i.e., 1728 points in the first Brillouin zone. The G_{max} and RK_{max} values were selected as 16 $(a.u.)^{-1}$ and 7.5, respectively.

The material's electronic properties, which exhibit semiconductor characteristics, were also supported using the GGA + mBJ approximation [32]. Elastic calculations were then performed using the IRElast software, developed by Jamal et al. and integrated with the Wien2k program, to prove the structural stability of the material [33]. Thermodynamic properties were determined using the Gibbs2 software, developed by Otero-de-la Roza et al. [34, 35]. External pressure values were selected between 0 and 10 GPa in 2 GPa steps, and temperatures were determined between 0 and 1200 K in 100 K steps.

Results and discussion

Structural properties

To obtain the ground state values for the most stable the Ti_2MnCoS_2 semiconductor DHH alloy, the volume-energy curves given in Fig. 2 were drawn.

$$E = E_0(V) + \frac{BV}{B'(B'-1)}\left[B\left(1-\frac{V_0}{V}\right)+\left(\frac{V_0}{V}\right)^{B'}-1\right] \quad (1)$$

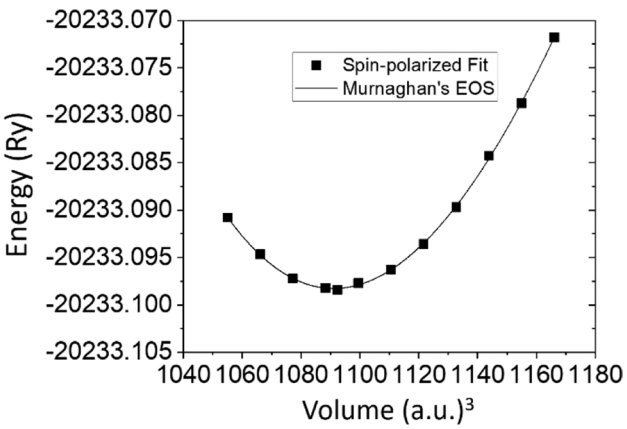

Figure 2 The calculated volume-energy curves of the Ti_2MnCoS_2 double half-Heusler alloy.

These curves were fitted with Murnaghan's equation of state [36], which is given in Eq. 1.

Based on the most stable state identified, the equilibrium lattice parameters of the Ti_2MnCoS_2 semiconductor DHH alloy were determined as a = b = 5.48 Å and c = 10.96 Å. The volume and energy values were 1090.9963 (a.u.)^3 and -20,233.09827 Ry, respectively, while the bulk modulus in the ground state was calculated as 173.437 GPa, as shown in Table 1.

Electronic properties

The Ti_2MnCoS_2 DHH alloy's electronic properties, whose structural properties have been determined, have been investigated using both GGA and GGA + mBJ approximations. Although the electronic properties of the Ti_2MnCoS_2 double half-Heusler alloy were calculated using the spin-polarized system, due to the 100% symmetry between the minority and majority electrons, the electronic properties are not given separately. The resulting electronic band structures and total densities of states are shown in Fig. 3.

As seen in Fig. 3, the Ti_2MnCoS_2 alloy exhibited semiconducting characteristics in both approximations. Here, the valence band maximum (VBM) values are above the Fermi energy levels at the N-points. The conduction band minimum (CBM) values are also above the Γ points in the GGA and GGA + mBJ approximations. The Ti_2MnCoS_2 alloy has an indirect band gap in both approximations. It can be easily observed that the CBM value is in the higher energy region when the GGA + mBJ approximation is used compared to the GGA approximation. In the GGA and

Table 1 The ground state values of the Ti_2MnCoS_2 double half-Heusler alloy

Structure	a = b (Å)	c (Å)	Volume (a.u.)^3	B (GPa)	B'	Energy (Ry)
Ti_2MnCoS_2	5.48	10.96	1090.9963	173.437	5.41	− 20,233.09827

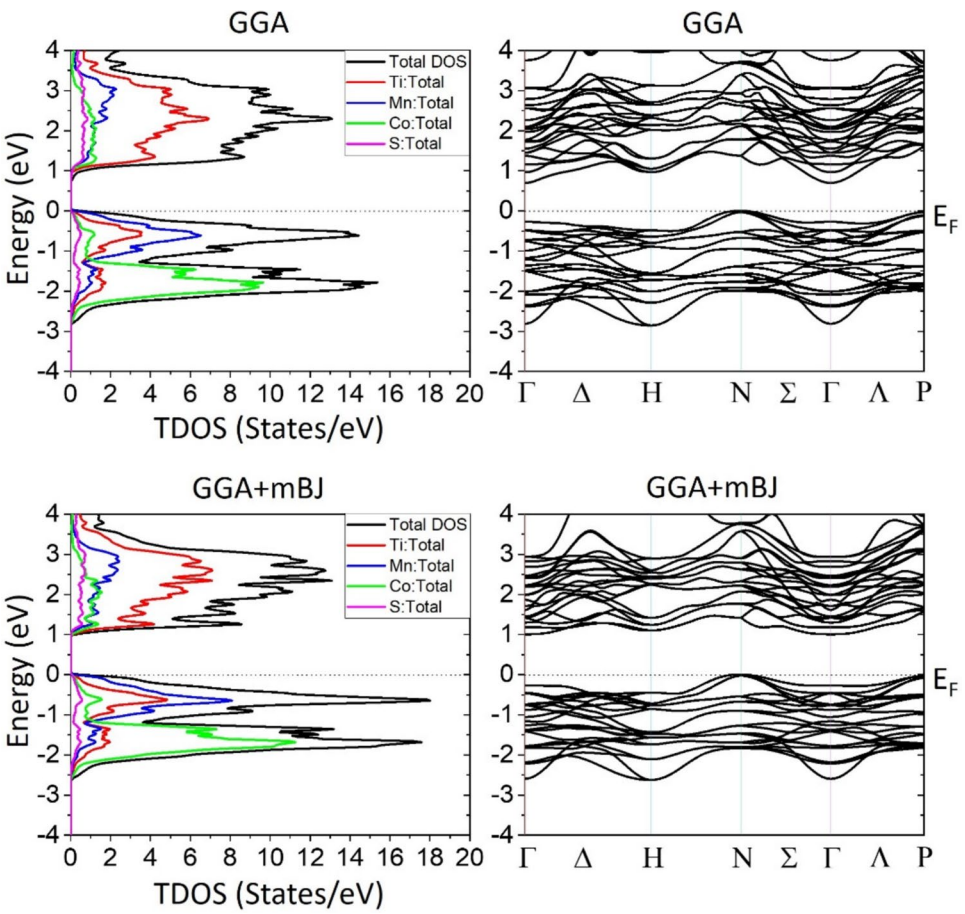

Figure 3 The plotted band structures and total densities of states of the Ti_2MnCoS_2 double half-Heusler alloy using GGA and GGA + mBJ approximations.

GGA + mBJ approximations, the VBM values are at 0 eV, i.e., lying in proximity to the Fermi energy level, while the CBM values are at 0.840 eV and 1.007 eV, respectively. Consequently, the Ti_2MnCoS_2 double half-Heusler alloy is obtained as a semiconductor material with band gaps of 0.840 eV and 1.007 eV under the GGA and GGA + mBJ approximations. When examining the total density of states, it is clear that the largest electron densities come from the transition metals Ti, Mn, and Co. In the valence band region, contributions from the Co atom are most intense between -1 eV and -2 eV. As the Fermi energy level approaches, contributions from the Mn and Ti atoms become more concentrated. In the conduction band, the main electron densities come from the Ti atom.

Elastic properties

The electronic structure of the Ti_2MnCoS_2 semiconductor DHH alloy was investigated to determine its resistance to structural deformation. The elastic properties of the DHH alloy were also investigated. The elastic stability conditions for tetragonal structures are given in Eq. 2 [37].

$$C_{11} > C_{12}; 2C_{13}^2 < C_{33}(C_{11} + 2C_{12}); C_{44} > 0; C_{66} > 0 \quad (2)$$

The results obtained are given in Table 2. According to Table 2, the Ti_2MnCoS_2 double half-Heusler alloy exhibits elastic stability and deformation resistance.

The bulk modulus value obtained from the elastic calculations is 165.6550 GPa. This value is very close to the value (173.4365 GPa) obtained from the ground state calculations. Therefore, the elastic calculations support the ground state calculations. The calculations given in Eq. 3 and 4 determine the Cauchy pressure (C_p) values of tetragonal materials [38].

$$C_p = C_{12} - C_{66} \quad (3)$$

$$C_p = C_{13} - C_{44} \quad (4)$$

Accordingly, the Cauchy's pressure values of the Ti_2MnCoS_2 semiconductor DHH alloy are 20.921 GPa and 21.338 GPa, respectively. Young's modulus, which represents the hardness of the material, was obtained at 217.325 GPa, while Poisson's ratio was calculated at 0.281. Positive Cauchy values and Poisson's ratio of 0.281 indicate that the Ti_2MnCoS_2 semiconductor DHH alloy is ductile [39, 40]. The

Table 2 The calculated elastic properties of the Ti_2MnCoS_2 semiconductor double half-Heusler alloy

Structure	C_{11} (GPa)	C_{12} (GPa)	C_{13} (GPa)	C_{33} (GPa)	C_{44} (GPa)	C_{66} (GPa)	C_{12}-C_{66} (GPa)	C_{13}-C_{44} (GPa)	B (GPa)	E (GPa)	ν
Ti_2MnCoS_2	252.361	121.02	122.447	254.379	101.109	100.099	20.921	21.338	165.655	217.325	0.281

material would be considered brittle if the Cauchy pressure value were negative and the Poisson's ratio were less than 0.26. Based on the variations in elastic moduli obtained using the values of the elastic constants C_{ij} given in Table 2, the minimum and maximum values of the Young modulus are between 173.5 GPa and 251.36 GPa. The shear modulus of the Ti_2MnCoS_2 semiconductor DHH alloy at equilibrium is 84.803 GPa, while the maximum and minimum values are 101.11 GPa and 65.459 GPa. The maximum and minimum values of the Poisson ratio, which plays a role in determining ductility and brittleness, are 0.42361 and 0.12192, respectively.

The Debye temperature of the Ti_2MnCoS_2 semiconductor DHH alloy was calculated 543.076 K using Eq. 5 [41].

$$\theta_D = \frac{\hbar}{k_\beta}\left[\frac{3nN_A\rho}{4\pi M}\right]V_m \tag{5}$$

$$V_m = [\frac{1}{3}(2V_t^{-3} + V_l^{-3}] \tag{6}$$

$$V_t = \sqrt{\frac{G}{\rho}} \tag{7}$$

$$V_l = [\frac{3B + 4G}{3\rho}]^{\frac{1}{2}} \tag{8}$$

Here, V_m is the typical sound velocity. V_m was calculated using Eq. 6 [42]. In Eq. 6, V_t and V_l represent the transverse and longitudinal velocities, respectively. These velocities were calculated by Eq. 7 and 8 as 3918.043 m/s and 7103.164 m/s, respectively [43].

Optical properties

The optical properties of the Ti_2MnCoS_2 semiconductor DHH alloy, which has been proven resistant to structural deformation, were also investigated in the photon energy range from 0 to 10 eV. The alloy's real and imaginary dielectric tensors, real optical conductivity, absorption coefficient, electron energy loss, optical reflectivity, refractive index, and extinction coefficient properties were investigated using the GGA and GGA + mBJ approximations. In Fig. 4, the alloy's real and imaginary dielectric tensors are given. These tensor functions illustrate how the wavelengths of incident light impact the optical properties of materials and are defined by Eq. 9 [44, 45].

$$\varepsilon(\omega) = \varepsilon_1(\omega) + i\varepsilon_2(\omega) \tag{9}$$

Figure 4 shows the high agreement between the GGA and GGA + mBJ approximations. According to Fig. 4, the static real dielectric tensor $\varepsilon_1(0)$ is obtained as 23.325 and 22.292 for the GGA and GGA + mBJ approximations, respectively. Subsequently, a monotonous sharp increase occurs in the GGA and GGA + mBJ approximations up to photon energy values of 1.565 eV and 1.537 eV, close to the visible light energy value (1.6 eV). The maximum peaks at these photon energy values are 38.703 and 37.213 for the GGA and GGA + mBJ approximations, respectively.

After these maximum peaks, sharp decreases occur. At 3.170 eV, the photon energy point is very close to the upper limit of the visible energy value (3.1 eV), and the real dielectric tensor value drops to a negative value. The material exhibits metallic characteristics between 3.1 eV and 5.701 eV because it reflects the incident radiation in this negative energy region.

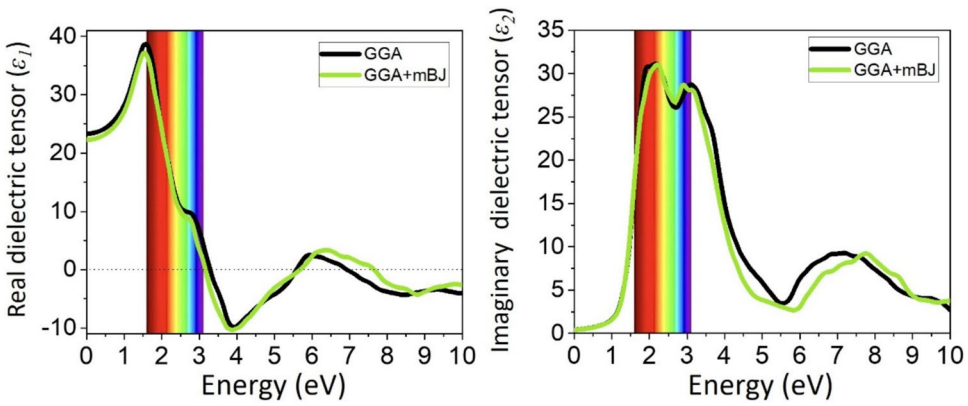

Figure 4 The obtained real (ε_1) and imaginary (ε_2) dielectric tensors of Ti_2MnCoS_2 semiconductor double half-Heusler.

Figure 5 shows the real optical conductivity (σ) and absorption coefficient (α) curves of the Ti_2MnCoS_2 semiconductor DHH alloy.

Optical conductivity (σ) and absorption coefficient (α) values of the Ti_2MnCoS_2 semiconductor DHH were calculated using Eqs. 10 and 11 [46].

$$\sigma(\omega) = \frac{\omega}{4\pi}\varepsilon_2(\omega) \tag{10}$$

$$\alpha(\omega) = \left(\frac{\sqrt{2\omega}}{c}\right) \times \left[\sqrt{\left(\varepsilon_1 2(\omega) + \varepsilon_2 2(\omega)\right)} - \varepsilon_1(\omega)\right]^{1/2} \tag{11}$$

Real optical conductivity exhibits sharp increases in the visible light energy range. The maximum peak value of 12,321.2 (1/Ohm cm) was obtained at a photon energy of 3.279 eV, near the upper limit of the visible light energy range. From this energy value, a sharp decrease is observed to 5.510 eV, at which point the real optical conductivity value is 2574.64/Ohm.cm. According to the absorption coefficient, there is an increase in regions near the lower limit of the visible light energy range. In contrast, the energy value at which the first maximum value is obtained is 3.850 eV. Here, the maximum absorption coefficient value is 152.998×10^4/cm.

Figure 6 shows the electron energy loss (L) curves of the Ti_2MnCoS_2 semiconductor DHH alloy using the GGA and GGA + mBJ approximations and Eq. 12 [47].

$$L = \frac{\varepsilon_2(\omega)}{\varepsilon_1^2(\omega) + \varepsilon_2^2(\omega)} \tag{12}$$

There is a slight increase in the initial and final peak limits of the visible light region. These values are 0.01001 and 0.03408, respectively. However, the sharpest peaks are in the energy region, far from the visible light region. For the GGA and GGA + mBJ approximations, these energy values are 5.565 eV and 5.728 eV, respectively, while the electron energy loss values at these energies are 0.287 and 0.357, respectively.

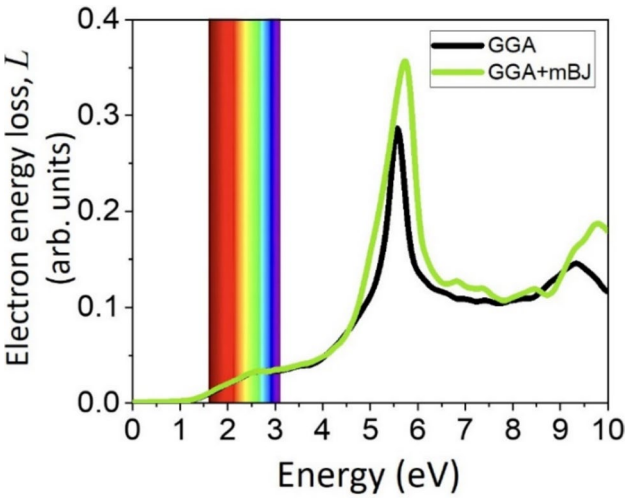

Figure 6 The obtained electron energy loss (L) of the Ti_2MnCoS_2 semiconductor double half-Heusler.

Figure 7 shows the optical reflectivity (R) curves of the Ti_2MnCoS_2 semiconductor DHH alloy obtained using the GGA and GGA + mBJ approximations. Although the curves for both approximations appear quite similar, the maximum and minimum peak values belong to the GGA + mBJ approximation. At 0 eV, the GGA and GGA + mBJ values are 0.4316 and 0.4231, respectively. As can be seen, the initial peak values are almost identical. There is a monotonic increase as one approximates the visible light energy region.

At the visible light initial limit, these values are 0.548 and 0.542. As can be seen, no difference is observed. This region exhibits small fluctuations in the GGA and GGA + mBJ approximations, reaching maximum values at 3.959 eV and 4.122 eV, respectively,

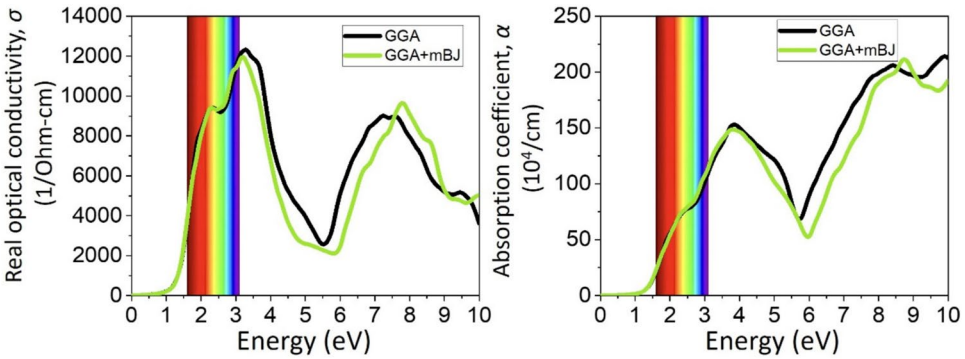

Figure 5 The obtained real optical conductivity (σ) and absorption coefficient (α) of the Ti_2MnCoS_2 semiconductor double half-Heusler.

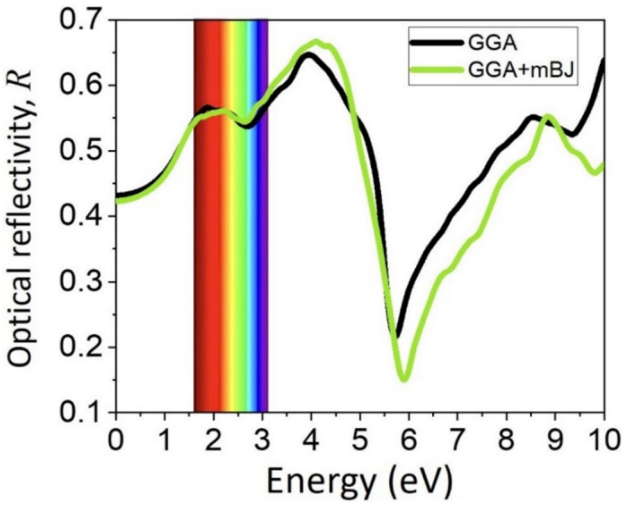

Figure 7 The obtained optical reflectivity (R) of the Ti_2MnCoS_2 semiconductor double half-Heusler alloy.

and decreasing to minimum values at 5.728 eV and 5.919 eV. Optical reflectivity values at maximum peaks are 0.647 and 0.667, while optical reflectivity values at minimum peaks are 0.216 and 0.151.

Figure 8 shows the refractive index (n) and extinction coefficient (k) of the Ti_2MnCoS_2 semiconductor DHH alloy. These curves were obtained using Eqs. 13 and 14 [48, 49].

$$n(\omega) = \frac{1}{\sqrt{2}}\left[\varepsilon_1 + \sqrt{\left(\varepsilon_1^2 + \varepsilon_2^2\right)}\right]^{1/2} \tag{13}$$

$$k(\omega) = \frac{1}{\sqrt{2}}\left[-\varepsilon_1 + \sqrt{\left(\varepsilon_1^2 + \varepsilon_2^2\right)}\right]^{1/2} \tag{14}$$

The refractive index has a wide range of meanings, encompassing various areas such as solar cells, sensors, and photonics [50, 51]. As can be seen, the curves are almost identical in both approximations. These two properties are not significantly different in the two different approximations. The initial peak value of the refractive index is 4.830 and 4.722 in the GGA and GGA + mBJ approximations, respectively. Although they are quite close, this value is larger in the GGA approximation. The refractive index increases sharply up to the initial limit of visible light. In fact, the maximum peak in the photon energy range of 0–10 eV is the initial limit of the visible light region. These values are 6.369 and 6.227 in the GGA and GGA + mBJ approximations, respectively. After this value, the refractive index decreases. This decrease continues up to 5.374 eV in the GGA approximation and up to 4.803 eV in the GGA + mBJ approximation. Although fluctuating increases occur thereafter, the maximum value is at the initial limit of the visible light region. The extinction coefficient is nearly zero at the initial values for both approximations. Then, it increases monotonically. It reaches its maximum peak value at photon energies of 3.74 eV and 3.60 eV, corresponding to 3.985 and 3.940 eV for the GGA and GGA + mBJ approximations, respectively.

Thermodynamic properties

The thermodynamic properties of the Ti_2MnCoS_2 semiconductor DHH alloy were investigated over a temperature range of 0 to 1200 K and an external pressure range of 0 to 10 GPa. The volume change curve for the Ti_2MnCoS_2 semiconductor DHH alloy is shown in Fig. 9. As the temperature increases, the volume increases, but it decreases with increasing pressure.

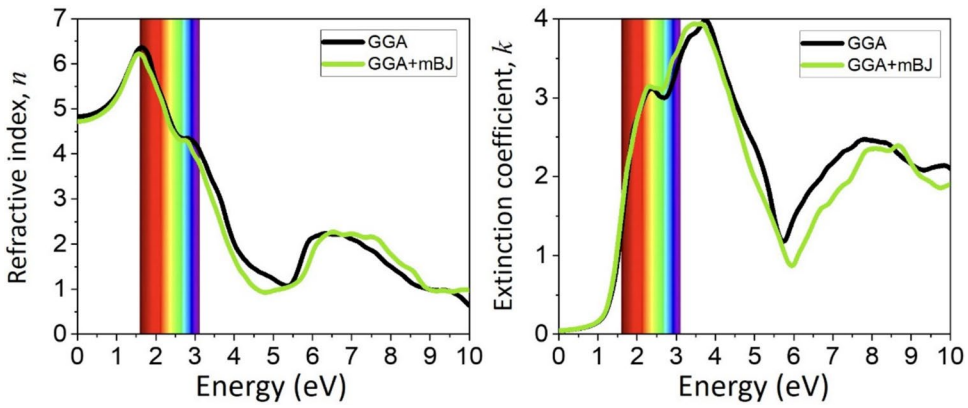

Figure 8 The refractive index (n) and extinction coefficient (k) of Ti_2MnCoS_2 semiconductor double half-Heusler alloy were obtained.

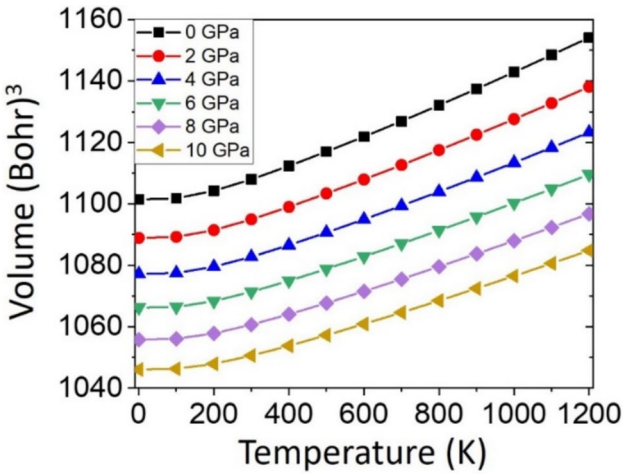

Figure 9 The obtained volume curves of the Ti_2MnCoS_2 semiconductor double half-Heusler alloy.

According to ground state calculations (0 GPa and 0 K), the equilibrium volume value was obtained as 1090.9963 (a.u.)^3. When the thermodynamic calculations were performed with initial values, the volume was calculated to be 1101.4132 (Bohr)^3. As these calculations seem, both volume values are almost the same. The maximum volume value was 1154.142 (Bohr)^3 at 0 GPa pressure and 1200 K temperature.

Thermodynamic comparisons of bulk modulus are made in Fig. 10. Here, the bulk modulus increases as pressure increases, while increasing temperature decreases the bulk modulus values. Compared with Fig. 9, it is evident that increasing volume values with temperature decrease the resistance to volume change shown in Fig. 10. The bulk modulus value at an external pressure of 0 GPa and a temperature of 0 K is 169.752 GPa. This result is between the bulk modulus value (173.437 GPa) obtained at the base state and the bulk modulus (165.655 GPa) obtained from elastic calculations. In other words, the values obtained by these three calculation methods are quite close. This shows that structural stability is preserved in all calculation approaches. The maximum bulk modulus value was obtained as 220.472 GPa at a pressure of 10 GPa and a temperature of 0 K.

Figure 11 shows the Gibbs energy curves. At 0 GPa and 2 GPa external pressures, the Ti_2MnCoS_2 semiconductor DHH alloy has negative Gibbs energy values at all temperatures except 700 K and 1000 K. These negative values indicate that the Ti_2MnCoS_2 semiconductor DHH alloy maintains its structural stability at all other temperatures.

As pressure increases, the absolute values of the Gibbs energy increase. While the values for all pressures concentrate at almost the same Gibbs energy value at 100 K, changes and separations are observed with increasing temperature. At pressures of 4 GPa, 6 GPa, 8 GPa, and 10 GPa and a constant temperature of 1200 K, the Gibbs energy values were obtained as − 0.00373 kJ/mol, − 0.01290 kJ/mol, − 0.01982 kJ/mol, and − 0.02421 kJ/mol, respectively.

Figure 12 shows the heat capacity and entropy changes of the Ti_2MnCoS_2 semiconductor DHH alloy. Both properties increase sharply to a temperature of

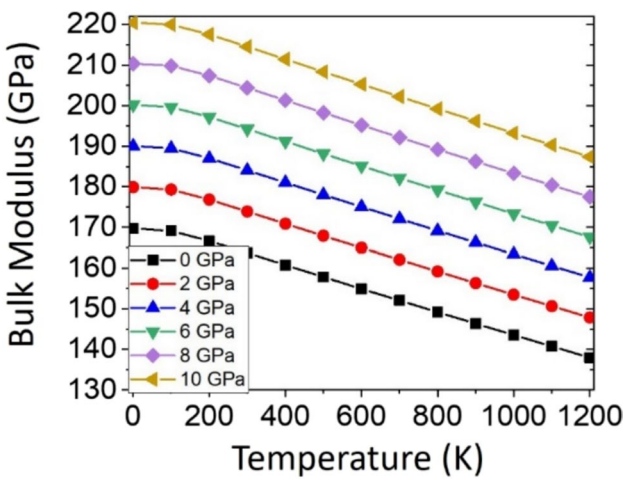

Figure 10 The obtained bulk modulus of the Ti_2MnCoS_2 semiconductor double half-Heusler alloy.

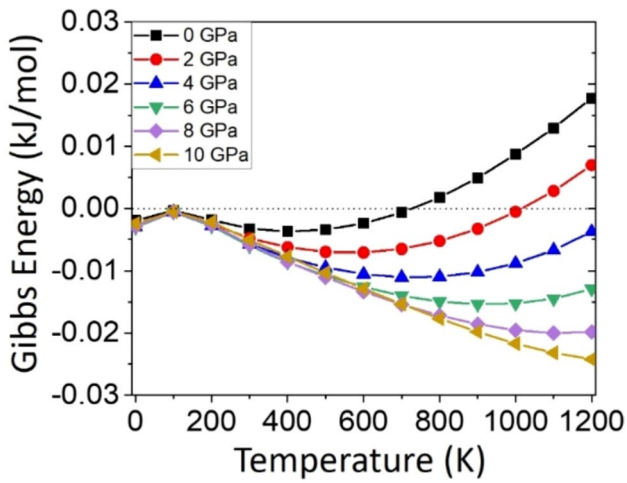

Figure 11 The obtained Gibbs energy curves of the Ti_2MnCoS_2 semiconductor double half-Heusler alloy.

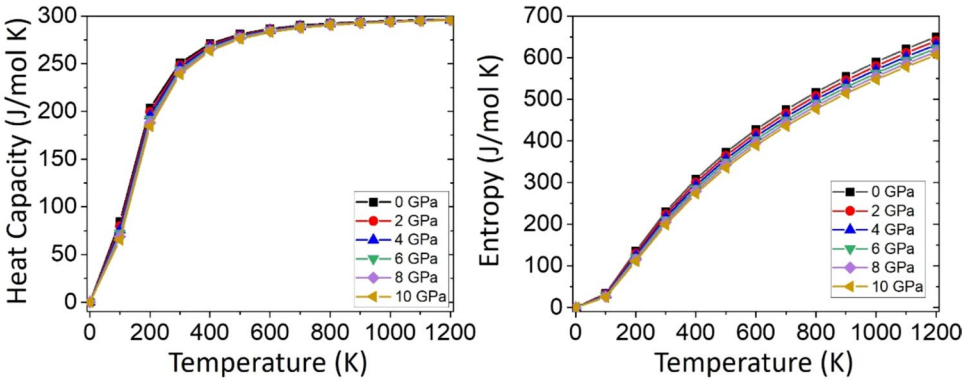

Figure 12 The obtained heat capacity and entropy of the Ti_2MnCoS_2 semiconductor double half-Heusler alloy.

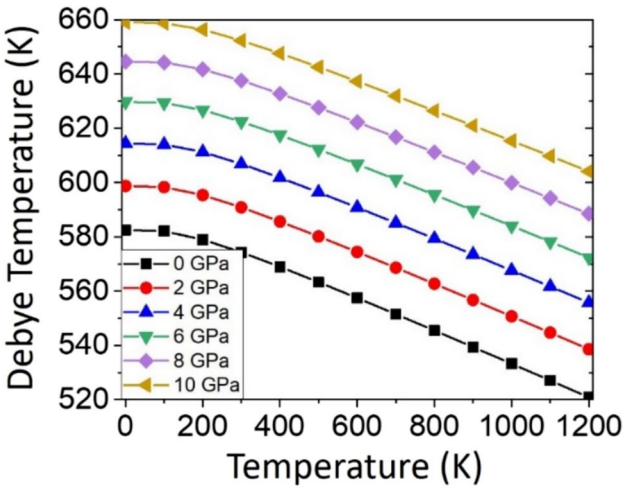

Figure 13 The obtained Debye temperature of the Ti_2MnCoS_2 semiconductor double half-Heusler alloy.

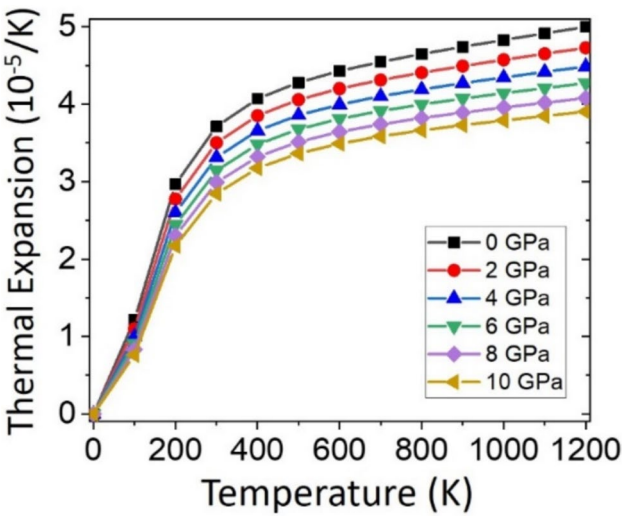

Figure 14 The obtained thermal expansion of the Ti_2MnCoS_2 semiconductor double half-Heusler alloy.

100 K, followed by a gradual increase with further temperature increases. According to the heat capacity curve, the increase in heat capacity decreases after 200 K. After approximately 900 K, the heat capacity value converges to a constant value of 295 J/mol K for all pressure values. At subsequent values, the increase is almost negligible. Although increasing pressure decreases the heat capacity values, these values are quite close in the Ti_2MnCoS_2 semiconductor DHH alloy. A similar situation applies to the entropy curve. Increasing pressure values decrease the disorder. However, all values are almost identical. The pressure increase does not clearly differentiate the entropy changes.

According to Fig. 13, the Debye temperature values of the Ti_2MnCoS_2 semiconductor DHH alloy increase with increasing pressure and decrease with increasing temperature. At 0 K and 0 GPa, the Debye temperature is 582.57 K. The maximum Debye temperature is at 0 K and 10 GPa external pressure. The Debye temperature value here is 659.13 K. The Debye temperature value (582.57 K) obtained from the initial state of thermodynamic calculations and the Debye temperature values (543.076 K) obtained from elastic calculations yielded similar results.

The thermal expansion curves for the Ti_2MnCoS_2 semiconductor DHH alloy are presented in Fig. 14. Thermal expansion refers to the increase in length and volume of the material with increasing temperature. Figure 9 shows that the volume of the material increases with increasing temperature. Therefore, as expected, thermal expansion increases with increasing temperature, while it decreases with increasing pressure. While sharp increases are observed at temperatures of 100 K and 200 K, the increase decreases after 200 K. In this study, the maximum value of

thermal expansion is 4.998×10^{-5}/K at a pressure of 0 GPa and a temperature of 1200 K.

Conclusion

The equilibrium lattice points of the Ti_2MnCoS_2 semiconductor DHH alloy are a = b = 5.48 Å and c = 10.96 Å. The alloy is most stable at these points. The bulk modulus is 173.4365 GPa. According to its electronic properties, the Ti_2MnCoS_2 semiconductor DHH alloy exhibits semiconducting behavior. In the valence band states near the Fermi energy level, the main contributions come from Mn atoms, while in the far energy region, they come from Co atoms. In the conduction band states, these contributions come primarily from Ti atoms. The net magnetic moment is zero in a spin-polarized system because the up and down states exhibit 100% symmetry. In the GGA and GGA + mBJ approximations, the VBM values are above the N-point Fermi energy levels. The CBM values are 0.840 eV and 1.007 eV at the Γ-points. Therefore, these values are also the band gap values of the Ti_2MnCoS_2 semiconductor alloy. The tetragonal Ti_2MnCoS_2 semiconductor DHH alloy provides elastic conditions. Therefore, the DDH alloy is resistant to deformation. The material is ductile because the Poisson's ratio is 0.281. The analysis of the optical properties using different approximations has yielded valuable insights that can inspire advancements in optical technologies. Consequently, the Ti_2MnCoS_2 semiconductor DHH alloy investigated in this study emerges as a promising material for applications in photonic and optoelectronic devices. The bulk modulus values obtained in thermodynamic, ground-state, and elastic calculations are very close. The Debye temperature values obtained from the initial state of thermodynamic calculations and those obtained from elastic calculations yielded similar results. This indicates that the calculations are internally consistent. Therefore, this suggests that the material is stable. In summary, the findings indicate that the examined materials possess remarkable functional characteristics, offering significant potential for advanced technological applications. This work is anticipated to provide meaningful insights and serve as a foundation for future investigations aimed at developing next-generation energy-harvesting and energy-conversion materials.

Funding

Open access funding provided by the Scientific and Technological Research Council of Türkiye (TÜBİTAK).

Data availability

Data will be made available on request.

Declarations

Conflict of interest The authors declare that they have no known competing financial interests or personal relationships that could have appeared to influence the work reported in this paper.

Open Access This article is licensed under a Creative Commons Attribution 4.0 International License, which permits use, sharing, adaptation, distribution and reproduction in any medium or format, as long as you give appropriate credit to the original author(s) and the source, provide a link to the Creative Commons licence, and indicate if changes were made. The images or other third party material in this article are included in the article's Creative Commons licence, unless indicated otherwise in a credit line to the material. If material is not included in the article's Creative Commons licence and your intended use is not permitted by statutory regulation or exceeds the permitted use, you will need to obtain permission directly from the copyright holder. To view a copy of this licence, visit http://creativecommons.org/licenses/by/4.0/.

References

[1] Heusler F (1903) Uber magnetische manganlegie rungen. Verh Dtsch Phys Ges 5:219

[2] Heusler F, Starck W, Haupt E (1903) Magnetisch-chemische studien. Verh Dtsch Phys Ges 5:220

[3] Beenaben SS, Radha S, Srinivasan M, Klinton BK, Prasath M (2025) MnNiSi half-Heusler alloy: computational and experimental insights for energy harvesting and spintronic applications. Chem Phys Imp 10:100891. https://doi.org/10.1016/j.chphi.2025.100891

[4] El-Khoult A, Amer SM, Khovaylo V, Lychagina T, Nikolayev D, Bancheva-Koleva P, Petkov P, Adam AM (2025) Mechanical and crystallographic texture features of half-Heusler TiCoSb and based alloys. J Al Comp 1037:182539. https://doi.org/10.1016/j.jallcom.2025.182539

[5] Özdemir EG, Doğruer S (2021) The electronic, half-metallic, elastic, and magnetic properties of new PtWZ (Z = In, Tl, Sn, and Pb) half-Heusler alloys via GGA and GGA+mBJ methods. Phys Scr 96:125869. https://doi.org/10.1088/1402-4896/ac3fcd

[6] Saatçi B, Şarlı N, Özdemir EG, Merdan Z (2021) Bridge constant and atom between theoretical and experimental magnetism in Ni_2MnSb Heusler alloy: DFT and EFT studies. Philos Mag 101:501–516. https://doi.org/10.1080/14786435.2020.1844330

[7] Boudjeltia MA, Boudjelal M, Houari M, Aziz Z, Bentata S, Bouadjemi B, Abderrahim BM (2025) Exploring the structural, optoelectronic, transport, and thermoelectric properties of half-heusler KSrX (X = P, As) for optoelectronic, photovoltaic, and thermoelectric applications. Phys B Condens Matter 717:417824. https://doi.org/10.1016/j.physb.2025.417824

[8] Peng Q, Iram N, Sharma R, Kumar A, Alsubaie AS, Rehman J (2024) Ab-initio investigation of structural, electronic, thermoelectric and optical properties of full-Heusler X_2MnB (X = Ti, Zr) for energy harvesting applications. Inorg Chem Commun 170:113240. https://doi.org/10.1016/j.inoche.2024.113240

[9] Güleşci Kartal Y, Özdemir EG, Merdan Z (2022) Electronic, magnetic and elastic calculations on half-metallic Heusler Ti_2RuTl compound. Philos Mag 102:153–165. https://doi.org/10.1080/14786435.2021.1972176

[10] Jabar A, Idrissi S, Bahmad L (2024) Study of the physical properties of the full Heusler Nb2RuSi alloy using first-principles calculations. Sol St Com 381:115446. https://doi.org/10.1016/j.ssc.2024.115446

[11] Özdemir EG, Doğruer S, Merdan Z (2024) Electronic, magnetic, half-Metallic, pressure-induced elastic and curie temperature predictions of Zr_2RhTl Heusler alloy: DFT and EFT studies. Philos Mag 104:115–135. https://doi.org/10.1080/14786435.2023.2285031

[12] Merzouk I, Samih A, Sabbah H, El Fdil R, Salmani E, Khan MN, Fadil Z, Raorane CJ, Kim SC (2025) Exploring the structural, electronic, magnetic, mechanical, thermodynamic, and optical behavior of Mn_2TaS full-Heusler alloy via first-principles calculations. Phys B Condens Matter 717:417818. https://doi.org/10.1016/j.physb.2025.417818

[13] Ha CV, Keovongsa S, Reyes-Serrato A, Guerrero-Sanchez J (2025) Structural, electronic, and magnetic properties of bulk and (001) surfaces NaFeAs half-Heusler alloy: a first-principles study. Mater Chem Phys 343:130968. https://doi.org/10.1016/j.matchemphys.2025.130968

[14] Balmumcu FI, Özdemir EG, Merdan Z (2023) Structural, half-metallic, electronic, magnetic and pressure-induced elastic changes of PdVSi, PdVGe, PdVSn, and PdVSb alloys. J Mater Sci 58:5349–5361. https://doi.org/10.1007/s10853-023-08364-z

[15] Ben Zoubair A, Samih A, El Fdil R, Nfissi A, Es-Semyhy M, Salmani E, Fadil Z, Raorane CJ, Kim SC, Saadaoui S (2026) First-principles calculations to investigate structural, elastic, mechanical, electronic, magnetic and optical properties of CsCrTe and CsMnTe half-Heusler alloys with varying atomic arrangements. J Mol Graph Model 142:109196. https://doi.org/10.1016/j.jmgm.2025.109196

[16] Wang X, Zhang Y, Yuan Z, Wang W, Shi J, Li S, Chang Y, Peng Y (2025) Recent advances in MNiSn (M = Ti, Zr, Hf) and Hf-based half-Heusler thermoelectric materials. J Alloy Compd 1044:184404. https://doi.org/10.1016/j.jallcom.2025.184404

[17] El Kihel K, Jalal EM, El Bouziani M (2025) Equiatomic quaternary Heusler alloy CoFeTiSn: a mean-field study. J Magn Magn Mater 630:173447. https://doi.org/10.1016/j.jmmm.2025.173447

[18] Wei XP, Mei ZY, Liu X, Tao X (2024) Investigations on stability, Gilbert damping, electronic and magnetic properties along with Curie temperature for quaternary Heusler alloys CrTiCoZ. Results Phys 58:107512. https://doi.org/10.1016/j.rinp.2024.107512

[19] Sun XW, Wu H, Xu SG, Song T, Liu ZJ (2025) Enhancing the half-metallicity of equiatomic quaternary Heusler compound OsZrTiSi via atomic doping. J Magn Magn Mater 632:173517. https://doi.org/10.1016/j.jmmm.2025.173517

[20] Kumar R, Roy T, Shirai M, Gupta S (2025) Low-moment semiconducting properties of quaternary Heusler alloy CoRuTiSn. J Alloy Compd 1026:180530. https://doi.org/10.1016/j.jallcom.2025.180530

[21] de Groot RA, Mueller FM, van Engen PG, Buschow KHJ (1983) New class of materials: half-metallic ferromagnets. Phys Rev Lett 50:2024. https://doi.org/10.1103/PhysRevLett.50.2024

[22] Hassan MA, El-Khouly A, Elsehly EM, Almutib EN, Elshamndy SK, Serhiienko I, Argunov EV, Sedegov A, Karpenkov D, Pashkova D, Gorshenkov M, Novitskii A, Voronin A, Kostishyn N, Khovaylo V, Adam AM (2023) Transport and thermoelectric properties of melt spinning synthesized $M_2FeNiSb_2$ (M = Ti, Hf) double half Heusler alloys. Mater Res Bull 164:112246. https://doi.org/10.1016/j.materresbull.2023.112246

[23] Mekki H, Baaziz H, Charifi Z, Ghellab T, Genç AE, Uğur Ş, Uğur G (2023) Properties of the double half-heusler alloy $ScNbNi_2Sn_2$ with respect to structural, electronic, optical, and thermoelectric aspects. Solid State Commun 363:115103. https://doi.org/10.1016/j.ssc.2023.115103

[24] Ding H, Li X, Feng Y, Wu B (2022) Electronic structure, magnetism and disorder effect in double half-Heusler alloy $Mn_2FeCoSi_2$. J Magn Magn Mater 555:169367. https://doi.org/10.1016/j.jmmm.2022.169367

[25] Uğur G, Kushwaha AK, Güler M, Charifi Z, Uğur Ş, Güler E, Baaziz H (2021) Electronic structure, optical and vibrational properties of $Ti_2FeNiSb_2$ and Ti_2Ni_2InSb double half heusler alloys. Mater Sci Semicond Process 123:105531. https://doi.org/10.1016/j.mssp.2020.105531

[26] Hasan R, Jo S, Shi W, Lee SY, Seo WS, Theja VCS, Vellaisamy RAL, Kim KT, Kim S, Kim SW, Kim HS, Lee KH (2023) Atomic site-targeted doping in $Ti_2FeNiSb_2$ double half-Heusler alloys: zT improvement via selective band engineering and point defect scattering. J Alloy Compd 938:168572. https://doi.org/10.1016/j.jallcom.2022.168572

[27] Zhao Y, Li X, Wu Q, Feng Y, Wu B (2024) Exploring stable half-metallicity and magnetism of Cr-based double half-Heusler alloys and its high magnetoresistance ratio in magnetic tunnel junction. Mater Sci Semicond Process 178:108415. https://doi.org/10.1016/j.mssp.2024.108415

[28] Blaha P, Schwarz K, Madsen GKH, Kvasnicka D, Luitz J (2001) WIEN2k, An augmented plane wave plus local orbitals program for calculating crystal properties, Vienna University Technology, Austria, ISBN 3–9501031–1–2

[29] Blaha P, Schwarz K, Tran F, Laskowski R, Madsen GKH, Marks LD (2020) WIEN2k: an APW+lo program for calculating the properties of solids. J Chem Phys 152:074101. https://doi.org/10.1063/1.5143061

[30] Momma K, Izumi F (2011) VESTA 3 for three-dimensional visualization of crystal, volumetric and morphology data. J Appl Crystallogr 44:1272–1276. https://doi.org/10.1107/S0021889811038970

[31] Perdew JP, Burke K, Ernzerhof M (1996) Generalized gradient approximation made simple. Phys Rev Lett 77:3865. https://doi.org/10.1103/PhysRevLett.77.3865

[32] Tran F, Blaha P, Schwarz K (2007) Band gap calculations with Becke-Johnson exchange potential. J Phys: Cond Mat 19:196208. https://doi.org/10.1088/0953-8984/19/19/196208

[33] Jamal M, Asadabadi SJ, Ahmad I, Aliabad HAR (2014) Elastic constants of cubic crystals. Comput Mater Sci 95:592–599. https://doi.org/10.1016/j.commatsci.2014.08.027

[34] la Otero-de- Roza A, Abbasi-Pérez D, Luaña V (2011) Gibbs2: a new version of the quasiharmonic model code. II. Models for solid-state thermodynamics, features and implementation. Comput Phys Commun 182:2232–2248. https://doi.org/10.1016/j.cpc.2011.05.009

[35] la Otero-de- Roza A, Luaña V (2011) Gibbs2: a new version of the quasi-harmonic model code. I. Robust treatment of the static data. Comput Phys Commun 182:1708–1720. https://doi.org/10.1016/j.cpc.2011.04.016

[36] Murnaghan FD (1944) The compressibility of media under extreme pressures. Proc Natl Acad Sci U S A. https://doi.org/10.1073/pnas.30.9.244

[37] Born M, Huang K (1956) Dynamical theory of crystal lattices. Clarendon, Oxford

[38] Hedjar Y, Saib S, Munoz A, Rodriquez-Hernandez P, Bouarissa N (2021) A pseudopotential study of structural, mechanical, and lattice dynamics behavior of the binary intermetallic Yttrium Tristannide YSn_3. Phy Stat Sol B 258:2100219. https://doi.org/10.1002/pssb.202100219

[39] Filabovich AN, Lukoyanov AV, Povzner AA (2023) Electronic structure and elastic properties of double half-Heusler thermoelectric materials $MgXY_2Z_2$ (X=Zr/Hf, Y=Pd/Pt, Z=Bi/Sb). Physica B 669:415280. https://doi.org/10.1016/j.physb.2023.415280

[40] Özdemir EG, Doğruer S (2023) Electronic, magnetic, and pressure-induced elastic investigaments of MnY_2O_4 oxide spinel. Eur Phys J Plus 138:23. https://doi.org/10.1140/epjp/s13360-022-03645-z

[41] Kalsoom U, Kalsoom A, Hussain A, Eariq MA, Mirza M, Qureshi WA, Tariq M, Batool Z, Nisa M (2025) Density-functional theory based structural, mechanical, thermal, electronic, and thermoelectric properties of Zr_2XNiSb_2 (where X = Fe, Pd, Pt) double half-Heusler alloys. Physica B 700:416897. https://doi.org/10.1016/j.physb.2025.416897

[42] Muhammad I, Zhang JM, Ali A, Rehman MU, Muhammad S (2020) Structural, mechanical, thermal, magnetic, and electronic properties of the RhMnSb half-Heusler alloy under pressure. Mater Chem Phys 251:123110. https://doi.org/10.1016/j.matchemphys.2020.123110

[43] Elahmar MH, Rached H, Rached D, Khenata R, Murtaza G, Bin Omran S, Ahmed WK (2015) Structural, mechanical, electronic and magnetic properties of a new series of quaternary Heusler alloys CoFeMnZ (Z=Si, As, Sb): a first-principle study. J Magn Magn Mater 393:165–174. https://doi.org/10.1016/j.jmmm.2015.05.019

[44] Azadparvar M, Rahnamaye Aliabad HA, Özdemir EG (2023) Optoelectronic and thermoelectric properties of Sb_2S_3 under hydrostatic pressure for energy conversion. AIP Adv 13:065218. https://doi.org/10.1063/5.0151650

[45] Vahidi H, Rahnamaye Aliabad HA, Özdemir EG (2025) Optoelectronic, magnetic, EFG and NMR properties of

olivine-type $LiMPO_4$ (M = Fe, Mn, Co, Mg) cathodes for application in lithium-ion battery by DFT. Results Phys 77:108425. https://doi.org/10.1016/j.rinp.2025.108425

[46] Hussain S, Kumar A, Azeem W, Makasana J, Rekha MM, Chennakesavulu K, Pradhan P, Aggarwal T, Al-harbi FFA, Oza AD, Rehman JU (2025) Study of structural, electronic, elastic, thermodynamic, and optical properties of perovskite $BiJO_3$ (J = Al, Ga, and Sc) materials for solid state photovoltaic applications: a DFT insights. Mater Res Bull 192:113607. https://doi.org/10.1016/j.materresbull.2025.113607

[47] Jabeen N, Zafar S, Hussain A, Abdullah AI, Kumar A, Ahmad H (2025) A DFT analysis on the electronic, mechanical, optical, elastic, structural and thermodynamic properties of $XBiNb_2O_7$ (X = Cs, Rb, K and Na) for photovoltaic applications. Comp Cond Mat 44:e01063. https://doi.org/10.1016/j.cocom.2025.e01063

[48] Aliabad HAR, Arzefooni AA, Sadati SZ, Özdemir EG, Khosrojerdi P (2024) High-performance optoelectronic and thermoelectric properties of transparent conductors based on Tl_2O_3 under pressure. Sci Rep 14:9237. https://doi.org/10.1038/s41598-024-58657-9

[49] Ravindran P, Delin A, Johansson B, Eriksson O (1999) Electronic structure, chemical bonding, and optical properties of ferroelectric and antiferroelectric $NaNO_2$. Phys Rev B 59:1776. https://doi.org/10.1103/PhysRevB.59.1776

[50] Safa RKG, Aliabad HAR, Baghani HR, Özdemir EG, Arzefooni AA, Sadati SZ (2025) Optoelectronic, thermoelectric, and EFG of atomic nuclei of trityl-functionalized fullerene C_{60} using GGA and mBJ approximations. Physica B 704:417053. https://doi.org/10.1016/j.physb.2025.417053

[51] Aliabad HAR, Sadati SZ, Arzefooni AA, Haghighatjoo S, Özdemir EG (2025) The structural and optoelectronic properties of $CdIn_2Te_4$ at three different phases by applying mBJ and GGA approximations. Opt Quan Elect 57:27. https://doi.org/10.1007/s11082-024-07302-w

Publisher's Note Springer Nature remains neutral with regard to jurisdictional claims in published maps and institutional affiliations.